CCFE
CULHAM CENTRE FOR FUSION ENERGY

UK Atomic Energy Authority

UKAEA-CCFE-PR(19)58

M. Coleman, S. McIntosh

The design and optimisation of tokamak poloidal field systems in the BLUEPRINT framework

Enquiries about copyright and reproduction should in the first instance be addressed to the UKAEA
Publications Officer, Culham Science Centre, Building K1/0/83 Abingdon, Oxfordshire, OX14 3DB, UK. The United Kingdom Atomic Energy Authority is the copyright holder.

The design and optimisation of tokamak poloidal field systems in the BLUEPRINT framework

M. Coleman, S. McIntosh

This is a preprint of a paper submitted for publication in
Fusion Engineering and Design

The design and optimisation of tokamak poloidal field systems in the BLUEPRINT framework

M. Coleman[a,b,*], S. McIntosh[a,c]

[a] United Kingdom Atomic Energy Authority, Culham Science Centre, Abingdon, Oxfordshire OX14 3DB, United Kingdom
[b] Department of Engineering, University of Cambridge, Trumpington Street, Cambridge CB2 1PZ, United Kingdom
[c] ITER Organization, Route de Vinon-sur-Verdon - CS 90 046 - 13067 St Paul Lez Durance Cedex, France

Abstract

As part of our aim to develop a reactor design framework, we present here our solution for the optimisation of plasma equilibria and tokamak poloidal field systems. A 2-D, free boundary, ideal magneto-hydrodynamic plasma equilibrium solver is described. We use it within the BLUEPRINT reactor design framework to design the plasma equilibria and poloidal field coilsets for future fusion reactors. Plasma shape parameters (R_0, A, δ, κ) and integral parameters (I_p, β_p, l_i) are controlled for. Novel constrained optimisation procedures for the positions, and currents of the poloidal field coils are presented, in which we account for current, field, force, and positional constraints on the coils. A pulse length constraint is incorporated in the optimisation procedure in the case of pulsed reactors. We conclude by demonstrating our approach on a range of reactor concepts: single-null, double-null and negative triangularity tokamaks.

Keywords:
Systems codes, DEMO, plasma equilibria, magnets, design optimisation

1. Introduction

The design of fusion reactors is a complex and delicate exercise in resolving conflicting sets of requirements through careful compromise. The first step towards a reactor design is to find a simplified solution that meets a range of basic engineering and physics constraints. Existing systems codes [1, 2] are the reactor designer's most useful tool when searching for an initial reasonable reactor solution. Being 0/1-D in nature, however, these codes can only offer a limited insight into fusion reactor design. For a self-consistent design of a tokamak, even at the conceptual level, more sophisticated models are required.

More advanced fusion reactor design frameworks, such as MIRA [3] and BLUEPRINT [4], are being developed, which account for higher-order (2/3-D) reactor design aspects. One of the most important reactor design activities, after the systems code solution, is the design of the plasma equilibria and the tokamak poloidal field system. The plasma equilibria and the associated magnetic coils set the stage for many subsequent design and analysis activities, such as the design of the first wall and blanket, magnet power supplies, control system, etc. In this work we present the free boundary equilibrium solver module of the BLUEPRINT code [4], and several design optimisation algorithms which are used to automatically design the poloidal field system of tokamak reactors to meet a wide variety of plasma physics and engineering constraints.

It is important to be able to carry out this design activity for a fairly broad range of different reactor concepts. Ideally, this would cover concepts ranging from the typical EU-DEMO [5] single null (SN) and double null (DN) machines, to more exotic snowflake (SF), super-X (SX), X-divertor (XD) configurations [6, 7], right up to negative triangularity (NT) [8, 9] and spherical tokamaks (ST) [10]. In keeping with the BLUEPRINT code's mission to support multiple reactor concepts, we demonstrate the approach on a range of different tokamak configurations: SN, DN, and NT.

Since we intend to integrate the optimal design of reactor poloidal field systems into the design of reactors within a global reactor design framework, it is vital that the design optimisation be carried out rapidly. This will enable its integration into reactor optimisation loops, in turn enabling the expedient exploration of the design space for future fusion reactors.

The design optimisation of tokamak equilibria and poloidal field systems is a challenging multi-disciplinary problem a with a rich history in the field. Many authors have tackled this problem in the past [11–16], often with the design of future fusion reactors in mind, given its significance relative to the performance of the reactor (plasma), and the cost of the machine (magnetic coils). In our approach to this design challenge, we draws upon this literature while developing several novel aspects.

2. Tokamak reactor design considerations

A number of considerations relating the the reactor design come into play when desiging the plasma equilibrium and poloidal field system of a tokamak.

*Corresponding author. Tel.: +44 (0)1235 464 527
Email address: matti.coleman@ukaea.uk (M. Coleman)

Firstly, the performance of the plasma must be ensured relative to a reference operating scenario, which involves a variety of activities:

(i) shaping the plasma (e.g. to meet a specified elongation, κ, and triangularity, δ)
(ii) constraining its position (major radius, R_0, aspect ratio, A)
(iii) constraining certain plasma profiles, such as the safety factor, q, profile
(iv) constraining several desired integral values, such as the plasma current, I_p, poloidal beta, β_p, and the normalised internal inductance, l_i
(v) ensuring that the plasma can be initiated during the breakdown phase
(vi) ensuring that the desired pulse flat-top length, τ_{ft}, can be achieved, in the case of a pulsed reactor.

Note that the poloidal field system is not the only system involved in these activities. The plasma and the heating and current drive (H&CD) systems play important roles in points (iii) to (vi)[1].

Secondly, future tokamak reactors are typically designed to operate at high plasma currents for long pulses (or even steady-state), meaning that the resulting poloidal field systems rely upon high-current, superconducting coils that are often required to operate near their limits. This means that the resultant set of engineering and design considerations relating to the magnetic coils but also to other aspects of the tokamak must be addressed. This involves:

(i) constraining the coil currents, **I**, such that they do not exceed conductor current limits
(ii) ensuring that the peak poloidal fields in the coils, **B**, do not exceed design margins relating to superconductivity limits
(iii) constraining the forces acting on the coils, **F**
(iv) ensuring that the positions of the coils, **L**, are compatible with the specified maintenance approach, vacuum vessel port locations, and other equipment connected to the reactor vacuum vessel
(v) ensuring that the particle and heat fluxes on the first wall and the position of the divertor strike points are compatible with the design of the tokamak plasma-facing surfaces
(vi) ensuring that the stability of the plasma in the tokamak is acceptable.

A suitable poloidal field system capable of satisfying all of the above constraints must be designed. In this work, we focus principally on the coil constraints, (i) to (iv).

The design of the plasma-facing surfaces (first wall and divertor targets) is intrinsically linked to the design of the equilibria and poloidal field system. These aspects are only partially addressed in our procedure, since before being able to design the plasma-facing surfaces, we must first design a viable plasma equilibrium. This requires an iterative design procedure whereby the plasma equilibria and plasma-facing surface designs are iterated to ensure consistency. The design of the equilibria and poloidal field system should be revisited when the design of the plasma-facing surfaces is carried out in earnest; i.e. with appropriate scrape-off layer particle and heat flux calculations.

We do not tackle the issue of the vertical stablisation of the plasma here, which is nevertheless a crucial aspect in the design of tokamak equilibria, and in which the poloidal field system plays a central role. Our justification is as follows: concepts for vertically stabilising the plasma in future fusion machines rely on a vast range of diagnostic and control systems, as well as passive features, in particular the vacuum vessel's toroidally continuous conducting shells. It is, however, crucial to know where the vacuum vessel is in order to assess the stability of the plasma, and in order to position the vacuum vessel, it is necessary to position the first wall, for which an equilibrium design is required. Our approach is therefore to first design the plasma equilibrium and poloidal field coil system without considering vertical stability. In future work, we will aim to close this design loop, and include vertical stability considerations into the reactor design procedure in BLUEPRINT.

Given this, it is therefore particularly important that the feasibility of achieving a specified plasma elongation, κ, is checked in later, dedicated analyses.

3. The ideal MHD plasma equilibrium problem

The two-dimensional axisymmetric ideal magneto-hydrodynamic (MHD) plasma equilibrium in cylindrical coordinates (X, ϕ, Z) is the well-known Grad-Shafranov equation [17, 18], in which the contribution of external coil currents can be included:

$$\Delta^* \psi = -\mu_0 X J_\phi \tag{1}$$

$$J_\phi = J_{\phi,pl} + J_{\phi,coils} \tag{2}$$

$$J_{\phi,pl} = X\frac{\partial p(\psi)}{\partial \psi} + \frac{F(\psi)}{\mu_0 X}\frac{\partial F(\psi)}{\partial \psi} \tag{3}$$

where:

$\Delta^* \equiv \frac{\partial^2 \psi}{\partial Z^2} + X\frac{\partial}{\partial X}\left(\frac{1}{X}\frac{\partial \psi}{\partial X}\right)$ is the Grad-Shafranov operator
$\mu_0 = 4\pi \times 10^{-7}$ is the permeability of vacuum (in V.s/(A.m))
$\psi(X, Z)$ is the poloidal magnetic flux per radian (in V.s/rad)
$J_{\phi,pl}$ is the toroidal current density in the plasma (in A/m^2)
$J_{\phi,coils}$ is the toroidal current density in the coils (in A/m^2)
$p(\psi)$ is the plasma pressure profile (in Pa)
$F(\psi)$ is the toroidal magnetic field profile (in T.m), which is a function of the toroidal field, B_ϕ

For the control of integral plasma values, it is convenient to choose an alternative representation of the plasma current profile, following [19], which substitutes Equation 3:

$$J_{\phi,pl} = \begin{cases} \lambda\left(\beta_0 \frac{X}{R_0} + (1-\beta_0)\frac{R_0}{X}\right) g(\overline{\psi}, \boldsymbol{\alpha}) \;\; \forall (X,Z) \in \Omega_p \\ 0 \quad \text{elsewhere} \end{cases} \tag{4}$$

[1] In BLUEPRINT, we isolate the design of the poloidal field system from the design of the H&CD system by allocating certain requirements to the two systems separately. For instance, to achieve a specified pulse length, requirements to drive certain fractions of the plasma current are allocated to: (a) the plasma itself (boostrap fraction, f_{bs}); (b) the H&CD systems (f_{cd}); and (c) the poloidal field system (f_{Ohmic}).

where:

R_0 is a characteristic length, taken to be the reactor major radius (in m)

λ and β_0 are variables which affect plasma integral values

$g(\overline{\psi}, \boldsymbol{\alpha})$ is a function of the normalised poloidal magnetic flux, $\overline{\psi}$, (i.e. a flux function - see below).

$\overline{\psi}$ is 0 at the magnetic axis, and 1 at the plasma boundary:

$$\overline{\psi} = \frac{\psi - \psi_a}{\psi_b - \psi_a} \tag{5}$$

Common flux function parameterisations include double power functions, Lao polynomials [20], and Luxon exponentials [19] (see Equations 6, 7, and 8).

$$g(\overline{\psi}, \boldsymbol{\alpha}) = \left(1 - \overline{\psi}^{\,\alpha_1}\right)^{\alpha_2} \tag{6}$$

$$g(\overline{\psi}, \boldsymbol{\alpha}) = \sum_{n=0}^{N} \alpha_{n+1} \overline{\psi}^{\,n+1} - \overline{\psi}^{\,N+1} \sum_{n=0}^{N} \alpha_{n+1} \tag{7}$$

$$g(\overline{\psi}, \boldsymbol{\alpha}) = \exp\left(-\alpha_1^2 \overline{\psi}^{\,2}\right) \tag{8}$$

where $\boldsymbol{\alpha} = (\alpha_1, \alpha_2, .., \alpha_N)$ is the vector of flux function shaping parameters. In the following, a double power flux function parameterisation is used as it is usually appropriate for H-mode plasmas with high β_p and monotonically increasing q profiles. All of the above flux functions are available as options however, ensuring that hybrid and reversed shear regimes or more exotic plasma current profiles can be treated.

4. Free boundary equilibrium solver

The Grad-Shafranov equation has ψ terms on both sides, and is as such a non-linear problem.

Here, as with many other free boundary equilibrium codes, the problem is divided into two parts: a finite difference formulation of the plasma toroidal current, $J_{\phi,pl}$, and a "grid-free" calculation of the contributions from external coil currents, $J_{\phi,coils}$, using Green's functions to represent point current sources.

4.1. Finite difference solution to the Grad-Shafranov equation

It is standard practice in Poisson-type Grad-Shafranov solvers to treat the plasma in a discretised manner, as its position is not known *a priori* and the current distribution is non-uniform.

Equations 1 and 3 can be converted to a linear equation using a common second-order centred finite difference approach on a uniform rectangular n_x by n_z grid representing the domain, Ω_{FD}, as discussed in [21]. An identical scheme is followed here, see Equation 9 and Figure 1. For our purposes, moderate discretisation is appropriate; in the following we take $n_x = 65$ and $n_z = 65$.

$$\begin{aligned}
&\frac{1}{(\Delta Z)^2}\psi_{i-1,j} + \left(\frac{1}{(\Delta X)^2} + \frac{1}{2X_j(\Delta X)}\right)\psi_{i,j-1} \\
&+ \left(\frac{2}{(\Delta X)^2} + \frac{2}{(\Delta Z)^2}\right)\psi_{i,j} + \left(\frac{1}{(\Delta X)^2} - \frac{1}{2X_j(\Delta X)}\right)\psi_{i,j+1} \\
&+ \frac{1}{(\Delta Z)^2}\psi_{i+1,j} = -\mu_0 X_j J_{\phi,pl_{i,j}}
\end{aligned} \tag{9}$$

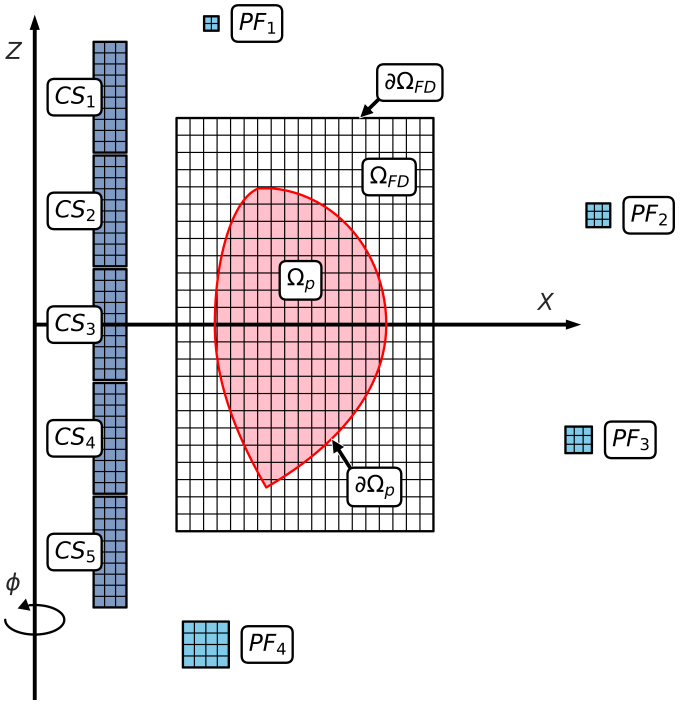

Figure 1: Diagram depicting the (X, ϕ, Z) coordinate system, the plasma domain and boundary, Ω_p and $\partial\Omega_p$, the finite difference domain and boundary, Ω_{FD} and $\partial\Omega_{FD}$ (here $n_x = 20$ and $n_z = 25$), and an example set of discretised external CS and PF coils, which haved been numbered and named *à la* ITER.

Equation 9 is then solved by reformulating it into a matrix problem (i.e. $\mathbf{Ax} = \mathbf{b}$) which is solved for $\mathbf{x}$, given the sparse Grad-Shafranov operator matrix, $\mathbf{A}$, and a known boundary term, $\mathbf{b}$, (to which a Dirichlet boundary condition is applied - discussed later).

The source term on the right-hand side, $J_{\phi,pl}$, is a strong function of the ψ term on the left-hand side. To resolve this non-linearity, a simple and commonly-used Picard iteration approach is employed, such that:

$$\Delta^* \psi^{[n]} = -\mu_0 X J^{[n]}_{\phi,pl}(\psi^{[n-1]}) \tag{10}$$

where n denotes the n-th Picard iteration. The iteration is terminated when the solution is converged, according to a user-specified criterion. Typically, we use $\frac{\max|\psi^{[n-1]} - \psi^{[n]}|}{\max(\psi^{[n]}) - \min(\psi^{[n]})} \leq 10^{-3}$, following [22], as this criterion is met fairly quickly and generally avoids the need for numerical vertical stabilisation.

4.2. Domain boundary conditions

The boundary condition at the edge of the finite difference domain is not constant, and changes at each iteration step.

A Dirichlet boundary condition is implemented such that at each iteration step ψ is specified at the finite difference domain boundary, $\partial\Omega_{FD}$, accounting for the (changing) plasma current:

$$\psi^{[n]}|_{\partial\Omega_{FD}} = \int_{\Omega_p} J^{[n]}_{\phi,pl}(\mathbf{P})\mathcal{G}^{\mathbf{P}}_{\psi}(\mathbf{p})d\Omega_p \quad \forall \mathbf{p} \in \partial\Omega_{FD} \tag{11}$$

4.3. Green's functions for external coils

The contributions of external coil currents are calculated using Green's functions for a point source with a toroidal current.

The ψ, B_x, and B_z contributions from a number n_C of external circular coils may be evaluated on the domain, at a position (X, Z) as:

$$\psi(X,Z) = \sum_{i}^{n_C} I_i \mathcal{G}^{\mathbf{P_i}}_{\psi}(X,Z) \tag{12}$$

$$B_x(X,Z) = \sum_{i}^{n_C} I_i \mathcal{G}^{\mathbf{P_i}}_{B_x}(X,Z) \tag{13}$$

$$B_z(X,Z) = \sum_{i}^{n_C} I_i \mathcal{G}^{\mathbf{P_i}}_{B_z}(X,Z) \tag{14}$$

Where $\mathcal{G}^{\mathbf{P}}_{\psi}$, $\mathcal{G}^{\mathbf{P}}_{B_x}$, and $\mathcal{G}^{\mathbf{P}}_{B_z}$ are Green's functions for ψ, B_x, and B_z for a unit current at position $\mathbf{P} \equiv (X_c, Z_c)$, see Appendix 1. The external coils can be discretised into many uniformly distributed point sources of current within a given location, for addition precision, also see Appendix 1. This is particularly important when dealing with high aspect ratio rectangular coils, such as those commonly found in central solenoids.

Note that the total poloidal magnetic flux can be calculated on Ω_{FD} simply by summing the contributions of the plasma (from solving Equation 9 for ψ) and the external coils (Equation 12).

4.4. Plasma boundary identification

The plasma boundary is identified by the relative positions and magnetic flux values of the various O-points, X-points, and limiter points.

First, an algorithm is used to find all the O- and X-points on the grid, which effectively finds the exact locations where:

$$|\nabla\psi|^2 = 0 \tag{15}$$

All local minima in $|\nabla\psi|^2$ on Ω_{FD} are found, with further searches using local minimisation techniques being conducted if the poloidal magnetic field is found to be below a certain low value, to find the exact locations of the magnetic null-field points.

The null-field points are then sorted into O- and X-points by the signs of their second derivatives, as per [23]:

$$S(\mathbf{P}) = \left(\frac{\partial^2\psi}{\partial X^2}\right)\left(\frac{\partial^2\psi}{\partial Z^2}\right) - \left(\frac{\partial^2\psi}{\partial X \partial Z}\right) \tag{16}$$

where a field null $\mathbf{P}$ is an O-point if $S(\mathbf{P}) > 0$ and an X-point if $S(\mathbf{P}) < 0$.

The O-point the closest to the desired plasma magnetic axis is selected, and the magnetic flux at this point is denoted ψ_a.

Then, the X-points and limiter points are sorted in ψ-space, in decreasing order from the point with magnetic flux closest to ψ_a.

To avoid picking up spurious X-points or limiters, the ordered list of points is searched again in order, to check that the evolution of ψ in space monotonically decreases from the O-point to the point in question, following an approach used in FreeGS [22]. The first such point fulfilling this condition is selected as the plasma delimiting point, and its magnetic flux is denoted as ψ_b.

The 2-D boundary of the flux surface crossing the plasma delimiting point, $\partial\Omega_p$, is used to denote the plasma region, Ω_p. A simple 2-D ray-tracing algorithm is used to populate a masking matrix, $\mathbf{M}$, on Ω_{FD}, such that:

$$\mathbf{M}_{n_x \times n_z} = \begin{cases} 1 & \text{if } \mathbf{p} \in \Omega_p \quad \forall \mathbf{p} \in \Omega_{FD} \\ 0 & \text{otherwise} \end{cases} \tag{17}$$

This matrix is used to bound the plasma current and pressure terms on the grid, ensuring that such terms are only non-zero inside Ω_p.

5. Application to reactor design

5.1. Design decisions

The reactor designer is presented with an important design decision early on: "Should one install the PF coils inside the TF coils, or vice versa?"

Generally speaking, the production of net electricity in a fusion power plant demands the use of cryogenically cooled superconducting coils to avoid large resistive losses[2].

Joints, and in particular separable joints, are extremely problematic for superconducting winding packs — due to the complexity of the underlying conductors and the requirement to achieve nano-Ohmic resistances in large surface areas of brazed joints. So, in order to avoid waiting for the full TF coil set to be manufactured and assembled before then threading the PF coil winding packs in-situ *through* the TF coils (which would be regrettable from a project management and assembly perspective), the PF coils are typically placed outside the TF coils. This places significant spatial constraints on the positions of the PF coils, which are considerably further away from the plasma than copper coils in many present-day machines.

Next the choice of superconductor must be made: low temperature superconductors (e.g. NbTi or Nb_3Sn) or high temperature superconductors (e.g. BSSCO or REBCO), which then impose practical field and winding pack current density constraints to be considered in the design of the poloidal field system. A typical decision is to use more expensive, higher current density materials (Nb_3Sn or HTS) for the central solenoid (CS),

[2]Cryogenically cooled normal conductors such as high purity Cu and Al can also be considered, and can to some extent relax constraints on the field at the coils (despite also exhibiting some magneto-resistive effects) and come, naturally, at the price of some resistive losses in the system.

resulting in higher flux swings which in turn enable longer flat-top durations. The PF coils are then often chosen to be made of cheaper, lower current density NbTi, given their much longer winding lengths and large volumes, and the fact that their size is less important to the minimisation of the reactor major radius.

We assume some default values for LTS materials: see Table 1. These values are taken over the entirety of the coil cross-section (i.e. they include conductor jacketing, insulation, copper, etc.) and are used throughout the rest of the paper.

Table 1: Default engineering constraints for LTS materials

	Nb_3Sn	NbTi
J_{max} [MA/m^2]	16.5	12.5
B_{max} [T]	13	11.5

The number of PF coils, n_{PF}, and the number of CS coils, n_{CS}, must be chosen (the total number of coils, $n_C \equiv n_{PF}+n_{CS}$). In theory, n_C could also be an optimisation variable, provided vertical stability effects are considered and appropriate optimisation techniques are used. However, we choose here to make this a decision in the hands of the reactor designer rather than an algorithm.

Finally, a sub-system design objective for the equilibrium and poloidal field system must be selected. Many options are valid here[3]. One can:

(i) minimise the error relative to the plasma physics constraints listed in Section 2
(ii) minimise the volume of magnets, weighted to the relative cost(s) of the magnet materials chosen (ersatz for capital cost)
(iii) minimise the total sum of the maximum currents in the coils (ersatz for capital and operational costs)
(iv) multiple objectives or weighted combinations of the above

5.2. Plasma integral constraints

The 1-D plasma current and pressure profile parameterisations must be chosen to satisfy some integral parameters based on a given reactor design. A typical approach, see e.g. [15, 24], is to constrain the plasma current, I_p, the ratio of the plasma pressure to the poloidal magnetic field pressure, β_p, and the normalised internal plasma inductance, l_i.

$$I_p = \int_{\Omega_p} J_\phi d\Omega_p \tag{18}$$

$$\beta_p = \frac{\langle p \rangle}{B_p^2/2\mu_0} = \frac{4}{\mu_0 R_0 I_p^2}\int_{\Omega_p} p d\Omega_p \tag{19}$$

$$l_i = \frac{4}{\mu_0 R_0 I_p^2}\int_{\Omega_p} \frac{\|B_p^2\|}{2\mu_0} d\Omega_p \tag{20}$$

From Equations 4 and 19, following an approach taken in [21], we can determine two of the unknowns, λ and β_0, thus ensuring that the I_p and β_p constraints are met, see Appendix 2.

[3]Bearing in mind that the global reactor cost should be optimised over the full reactor design sequence.

To enforce the l_i constraint, one must determine the shape parameters, $\boldsymbol{\alpha}$, of the selected flux function. As the plasma shape is irregular and varies during each iteration of the Grad-Shafranov solution, a minimisation problem is set up during each Grad-Shafranov iteration, in order to find the optimal shape parameter vector[4], $\boldsymbol{\alpha}^*$:

$$\boldsymbol{\alpha}^* = \underset{\boldsymbol{\alpha}}{\text{minimise}} : \left| l_{i_{target}} - \frac{4}{\mu_0 R_0 I_p^2}\int_{\Omega_p} \frac{\|B_p^2\|}{2\mu_0} d\Omega_p \right| \tag{21}$$

Constraints may be applied to $\boldsymbol{\alpha}$ in order to impose certain current and/or pressure profiles, and to improve convergence.

An alternative approach, taken e.g. by [16], is to forego the calculation detailed in Appendix 2, and optimise the profile and shape parameters to meet the $[I_p, \beta_p, l_i]$ constraints. This method has the advantage of being able to handle two flux function shapes as opposed to just the one.

5.3. Equilibrium constraints

Next, a series of constraints is defined to produce a desired plasma shape, which is traditionally implemented as a function of κ and δ.

An initial plasma boundary shape is calculated using the Johner parameterisation [25], which can handle single and double null plasma shapes, and can be made up-down, in-out asymmetric. The simpler, symmetric, Manickam plasma shape parameterisation [26] was also tested, but was generally found in the case of single nulls to lead to equilibria where the inactive null is positioned very close to the separatrix. This is undesirable most notably for plasma control and the design of the first wall, where large fractions of the scrape-off layer charged particle power is deposited in regions other than the divertor[5].

A set of n_T constraints are applied on the calculated plasma boundary, in the form of ψ, B_x, and B_z constraints. The ψ values are set to a desired value, ψ_b, at all points on the plasma boundary (typically ~40 to 150 points suffice), and a null field condition is specified at the X-point: $B_x = 0, B_z = 0$. One can also specify ψ constraints for the divertor legs, in order (for example) to ensure that the positions of the divertor strike points remain more or less fixed over the course of a pulse. Equations 12, 13, and 14 are used to set up an equation of the form:

$$\mathbf{GI} = \mathbf{b_t} - \mathbf{b_p} \tag{22}$$

where:

$\mathbf{G}$ is a $n_T \times n_C$ matrix of Green's functions evaluated at the control points
$\mathbf{I}$ is a n_C vector of external coil currents
$\mathbf{b_t}$ is a n_T vector of target values
$\mathbf{b_p}$ is a n_T vector of the contribution of the passive currents (including the plasma) to the desired constraints.

[4]In the following, we use the superscript * to indicate optimality.

[5]The Johner and Manickam parameterisations are usually sufficient for conventional plasma shapes, however less conventional shapes (e.g. highly triangulated, strongly asymmetric, etc) require additional parameterisations.

A general, unconstrained solution to this minimisation problem proves useful during the first few stages of non-linear iterations. As Zakharov [27] and Lackner [28] note, the problem of the determination of external currents to create an arbitrarily defined plasma shape constitutes an ill-posed problem in the sense of Hadamard. Following [27] and many others, we use Tikhonov regularisation [29] on the $\mathbf{L_2}$-norm of Equation 22 to determine an optimal set of currents, $\mathbf{I}^*$:

$$\mathbf{I}^* = \underset{\mathbf{I}}{\text{minimise}} : \quad ||\mathbf{GI} - \mathbf{b_t} + \mathbf{b_p}||_2^2 + ||\mathbf{\Gamma I}||_2^2 \tag{23}$$

where $\mathbf{\Gamma}$ is the regularisation term taken to be a small multiple ($\sim 10^{-7}$) of the identity matrix. In the following Equation 23 can be solved analytically as:

$$\mathbf{I}^* = (\mathbf{G}^\intercal\mathbf{G} + \mathbf{\Gamma}^\intercal\mathbf{\Gamma})^{-1}\mathbf{G}^\intercal(\mathbf{b_t} - \mathbf{b_p}) \tag{24}$$

Note that when attempting to fit a desired plasma separatrix shape, it can be useful to apply weightings to the $\mathbf{G}$ matrix and the $(\mathbf{b_t} - \mathbf{b_p})$ error vector, in particular when the fit around X-points (where $\nabla\psi$ is low) is otherwise poor. We find that setting weights on the ψ errors inversely proportional to the square of the poloidal field can be helpful in this context, following an approach suggested in [30].

5.4. Coil current, force, and field constraints

The central solenoid (CS) and poloidal field (PF) coils provide the external currents required to control the position and shape of the plasma. In order to design a tokamak's magnetic cage, it is important to respect the design constraints inherent to the CS and PF coils. The CS coils form part of the radial build of the reactor, and for consistency with the rest of the reactor design in the BLUEPRINT code, the thickness of the CS coils is held constant. Depending on the vertical extent of a CS coil, the maximum current, I_{max}, that a coil can safely carry is determined by an indicative current density for a coil winding pack: $I_{max} = A_{coil}J_{max}$. In principle, the PF coil currents are not constrained by current limits (as they could be made arbitrarily large, provided other constraints are met). In practice, however, it is convenient not to have overly large PF coils, so a current limit is specified for the PF coils as $I_{max} = \eta I_p$, where e.g. $\eta = 1.4$. The size of the PF coils is dynamically adjusted according to the maximum current required of them.

Superconductivity is fickle; in order to keep a material in a superconducting state, the field, current density, and temperature must be kept within an operational margin of certain material-dependent limits. The current density constraints are applied as discussed above, and the magnetic field at the coils is constrained to be below $\mathbf{B_{max}}$, the vector of maximum fields at the coils[6]. The temperature constraints are not addressed in this model; it is assumed that the coils operate at their nominal temperatures (which to some extent determines the value of J_{max}).

Large vertical $\mathbf{j} \times \mathbf{B}$ forces are generated in the coils which must be withstood by the coil cage structures[7]. In superconducting tokamaks, the CS and PF coils are often mechanically and thermally connected to the toroidal field (TF) coils, out of a desire to minimise the thermal conduction paths to a large cryogenic mass by connecting it to room temperature bodies at the fewest possible locations. Given this, the forces on the magnets must be resisted by the magnet cage as a whole, which is why, following [15], we apply maximum value constraints to the vertical force a single PF coil, total absolute vertical force on all CS coils, and the vertical separation forces between each module in the CS stack (tension only).

The aforementioned constraints can be applied to Equation 23 to give:

$$\begin{aligned}
\mathbf{I}^* = \underset{\mathbf{I}}{\text{minimise}} : \quad & ||\mathbf{GI} - \mathbf{b_t} + \mathbf{b_p}||_2^2 + ||\mathbf{\Gamma I}||_2^2 \\
\text{subject to} : \quad & |\mathbf{I}| \leqq \mathbf{I_{max}} \\
& \mathbf{B} \leqq \mathbf{B_{max}} \\
& |F_i| \leq F_{PF_{max}} \quad \text{for } i \in [1, .., n_{PF}] \\
& \Big|\sum_{j=1}^{n_{CS}} F_j\Big| \leq F_{CS_{tot_{max}}} \\
& \sum_{i=1}^{j} F_i - \sum_{i=j}^{n_{CS}} F_i \leq F_{CS_{sep_{max}}} \quad \text{for } j \in [1, .., n_{CS}]
\end{aligned} \tag{25}$$

This is a non-linear optimisation problem with a quadratic objective function and linear and quadratic constraints. A sequential least squares optimisation algorithm, SLSQP [31], implemented in NLopt [32], is used to solve Equation 25. Using the Jacobians of the objective and constraint functions greatly improve the algorithm's performance, see Appendix 2 for details.

Note that the field constraints should actually be applied over the entire cross-section of each coil, and not at individual locations. Such an approach is complicated by our choice of Green's functions over a finite element method and, furthermore, would significantly complicate the analytical calculation of the Jacobian of the field constraints. Instead, we choose to constrain the poloidal field at the centre of the inside edge of each coil, where the field is generally the highest.

5.5. Coil position optimisation and constraints

A key decision when designing fusion reactors is where to place the PF coils. While the ability to generate and control the desired plasma shapes is an important consideration, so too is the positioning of the ports and penetrations to the vacuum vessel, which cannot coincide with the toroidally continuous PF coils. Future fusion reactors will be remotely maintained and it is important to ensure adequate access to the in-vessel components through the magnetic cage and into the vacuum vessel. Both vertical maintenance (e.g. [33]) and horizontal sector

[6] In principle the maximum field constraint on a coil could be higher if it were carrying less current, as its margin to superconducting quench would be higher. We ignore this in our model, out of convenience and conservativism.

[7] The radial $\mathbf{j} \times \mathbf{B}$ forces are resisted by tension of the circular coils, giving rise to a hoop stress but generally not transferring the force to rest of the magnet cage and structure (provided the radial forces are uniformally distributed).

maintenance (e.g. [34]) approaches apply strong constraints to the positions of the PF coils, as do penetrations for H&CD and other auxiliary systems.

Albanese et al. [15] tackle the problem of the constrained optimisation of the position of the PF coils with an exhaustive search on a combination of potential coil positions, chosen from a finite set of acceptable positions. They apply some restrictions on the proximity between coils based on engineering judgement, reducing the total number of permutations that need to be explored.

Here, we adopt a different approach, choosing instead to optimise the coil positions along a basis function. For this we take as an input from the BLUEPRINT code the outer edge of the TF coil shape (which has been optimised to meet toroidal field ripple constraints), from which we take an offset spline as a basis along which to position the PF coils. This basis function is parameterised such that a PF coil position vector $\mathbf{L} \in [0, 1]$ maps to coil positions in X, Z space, see Figure 2.

The coil position constraints are implemented by introducing exclusion zones, segmenting the basis function along which the PF coils can be positioned. If a coil is in an exclusion zone at the start of the optimisation procedure, it is moved to the nearest acceptable position. Each coil is then fixed to its "track" segment, with individual lower and upper bounds (L_{min} and L_{max}) applied, see Figure 2. Note that this has a similar effect to the engineering judgement applied in the Albanese procedure, in that it effectively reduces the breadth of the optimisation problem.

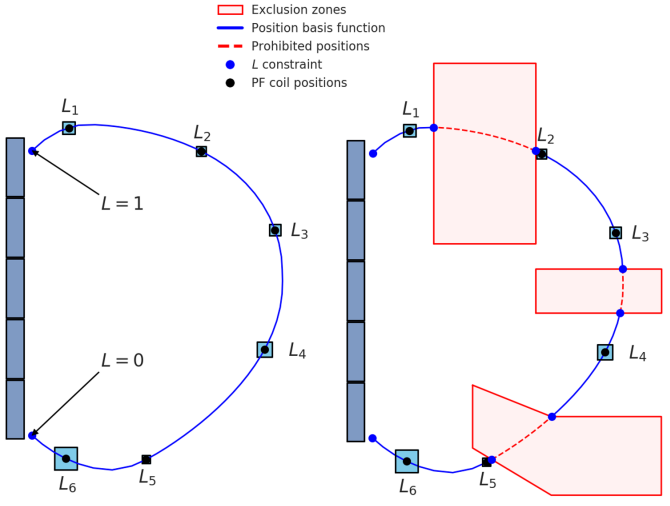

Figure 2: Diagram depicting the implementation of the coil position optimisation procedures (left); with no exclusion zones, and (right); with exclusion zones. Each PF coil is assigned an L value, with bounds L_{min} and L_{max}. The exclusion zones in this example were calculated in the BLUEPRINT code assuming a vertical maintenance approach.

For the central solenoid, a similar approach to the one described above is taken, except that we use a straight vertical line as the $\mathbf{L}$ vector basis and the divisions between the solenoid modules are optimised rather than their centre locations. The implicit design decision here is that the solenoid is a single vertical stack of multiple modules (with only minimal gaps between modules). The radius and thickness of the central solenoid are taken from the radial build of a systems code solution, and the vertical position and extent of the solenoid are calculated within the BLUEPRINT framework based on the size of the toroidal field coils. Often, however, a fairly regular spacing of modules in the central solenoid is desirable and reduces the dimensionality of the optimisation problem significantly.

The following optimisation problem is then solved, this time using the COBYLA optimisation algorithm [35], also implemented in NLopt [32]:

$$\begin{aligned} \mathbf{L}^* = \underset{\mathbf{L}}{\text{minimise}}: \quad & \|\mathbf{G}^{\mathbf{L}}\mathbf{I}^* - \mathbf{b_t} + \mathbf{b_p}\|_2^2 + \|\mathbf{\Gamma I}\|_2^2 \\ \text{subject to}: \quad & \mathbf{L} \geqq \mathbf{L_{min}} \\ & \mathbf{L} \leqq \mathbf{L_{max}} \end{aligned} \tag{26}$$

where:

$\mathbf{G}^{\mathbf{L}}$ is the $n_T \times n_C$ matrix of Green's functions evaluated at the control points with the coils at positions $\mathbf{L}$.

$\mathbf{I}^*$ is the optimal current vector for a given set of coil positions, calculated in Equation 25

$\mathbf{L_{min}}$ and $\mathbf{L_{max}}$ are the minimum and maximum normalised positions constraint vectors for the coils.

The gradients of the objective function are calculated numerically here, as $\mathbf{G}^{\mathbf{L}}$ is a complicated function of space. Generally speaking, fairly large ports are required for tokamak power reactors (for maintenance, service connections, and auxiliary systems). As such the positional constraints on the coils are quite strong, and actually make this optimisation step less onerous since less of the space must be searched.

5.6. Breakdown optimisation

The initiation of a plasma discharge in tokamaks is commonly carried out inductively. A toroidal electric field is induced by rapidly changing the current in the CS, while a multipolar magnetic null point is created in the centre of the machine[8], near the desired location of the plasma magnetic axis. This is a challenging dynamic problem in itself as the central solenoid currents are near their maxima, the currents in all coils must be accurately controlled over time, and induced currents in the vacuum vessel and structures and the operation of other tokamak systems can complicate matters. We simplify things here to consider only the most challenging part of the plasma discharge from the perspective of the poloidal field system. For our purposes, the breakdown phase is calculated by defining a region central to the desired plasma shape in which the poloidal field is close to zero. The aim is to maximise the magnetic flux at the centre of the machine, $\psi_{b_{BD}}$, so that the pulse can last as long as is desired. The engineering constraints on the coils are the same as described in Section 5.4. Here we set as an objective the maximisation of the CS coil currents (as an ersatz for the maximisation of the $\psi_{b_{BD}}$), and an optimisation problem is then solved:

[8] Although the breakdown phase is also often initiated near the wall, in larger future machines there is a desire to achieve breakdown without direct contact with limiters.

$$
\begin{aligned}
\mathbf{I}^* \;=\; \underset{\mathbf{I}}{\text{minimise}}: \quad & -\sum_{i=0}^{n_{CS}} |I_i| \\
\text{subject to}: \quad & \max(B_p|_{\Omega_{BD}}) \leq B_{p_{BD}} \\
& |\mathbf{I}| \leqq \mathbf{I_{max}} \\
& \mathbf{B} \leqq \mathbf{B_{max}} \\
& |F_i| \leq F_{PF_{max}} \;\; \text{for } i \in [1, .., n_{PF}] \\
& \Big|\sum_{j=1}^{n_{CS}} F_j\Big| \leq F_{CS_{tot_{max}}} \\
& \sum_{i=1}^{j} F_i - \sum_{i=j}^{n_{CS}} F_i \leq F_{CS_{sep_{max}}} \;\; \text{for } j \in [1, .., n_{CS}]
\end{aligned}
\tag{27}
$$

where Ω_{BD} is a circular region in the centre of the machine, of a radius r_{BD}, in which the maximum poloidal magnetic field must be below $B_{p_{BD}}$, typically ~ 3 mT for a large machine (see e.g. [36]).

This phase is particularly challenging for the **I**, **B**, and **F** constraints, with all three often being reached simultaneously across the coilset.

From the above, the magnetic flux at the time of the breakdown, $\psi_{b_{BD}}$, is taken as the flux at the the edge of Ω_{BD}. Note that $\psi_{b_{BD}}$ is determined with arbitrary PF coil positions, prior to the determination of $\mathbf{L}^*$. Experience has shown that this value does not depend much on the positions of the PF coil, and this step is repeated once optimal PF coil positions have been found, for consistency.

5.7. Considerations of pulsed operation

The flux at the plasma boundary at the start of the flat-top (SOF), $\psi_{b_{SOF}}$ can be calculated as:

$$
\psi_{b_{SOF}} = \psi_{b_{BD}} - \frac{\mu_0 R_0 l_i}{2} I_p - C_{Ejima} \mu_0 R_0 I_p \tag{28}
$$

where C_{Ejima} is a constant, taken as 0.4, following the literature [37].

For a pulsed reactor, the duration of flat-top is dictated by the time that the central solenoid can effectively induce a certain fraction of the plasma current. The classical design decision is to ramp the central solenoid currents from positive to negative values, in order to induce the necessary current in the plasma. The end of the pulse is thus dictated by the coilset as a whole, which must respect its engineering constraints. Here we implement the pulse length as a constraint, by fixing $\psi_{b_{EOF}}$:

$$
\psi_{b_{EOF}} = \psi_{b_{SOF}} - V_{burn} \tau_{ft} \tag{29}
$$

where V_{burn} is the plasma loop voltage during burn:

$$
V_{burn} = f_{ohmic} I_p R_p \tag{30}
$$

where f_{ohmic} is the fraction of Ohmic current drive, and R_p is the resistance of the plasma in Ohms.

Thus, for a pulsed reactor, Equation 25 must be solved for several different values of ψ_b. In practice, we solve it at the two most challenging points: at the start and end of the flat-top, where $\psi_b = \psi_{b_{SOF}}, \psi_{b_{EOF}}$, respectively. Intermediate values of ψ_b during the pulse can also be solved and optimised for. However, in the interests of computational speed we focus on cases which are typically limiting. If the fit to the specified plasma boundary is too poor for the end of flat-top phase, it implies that no solution is found for the specified number of PF and CS coils, and the specified constraints. The user is notified of this, so that the pulse length of the reactor can be modified accordingly or a new systems code run and radial build can be created to allow sufficient space for a central solenoid that can meet the pulse length constraint.

5.8. Summary of the optimisation procedure

In summary, in order to design the plasma equilibrium and poloidal field system to meet a specified set of R_0, A, κ, δ, β_p, l_i, and I_p, whilst constraining τ_{ft}, **F**, **B**, **I**, and **L**, multiple steps are required. First, a reference equilibrium is generated using unconstrained optimisation with a set of initial coil positions, see Equation 24.

For a pulsed tokamak, a breakdown optimisation step is carried out (Equation 27) to determine $\psi_{b_{BD}}$, from which $\psi_{b_{SOF}}$ (Equation 28) and $\psi_{b_{EOF}}$ (Equation 29) can be determined.

Then, in order to meet the τ_{ft}, **F**, **B**, and **I** constraints, a series of constrained optimisation problems are solved in a nested loop to determine the optimal coil locations $\mathbf{L}^*$ (Equation 26) across multiple equilibria over the course of a pulse, in which the optimal coil currents $\mathbf{I}^*$ (Equation 25) and flux function parameters $\boldsymbol{\alpha}^*$ are calculated (Equation 21). During this second step, the solution to the Grad-Shafranov equation is effectively treated as boundary condition. Once an appropriate $\mathbf{L}^*$ and set of $\mathbf{I}^*$ are found, the Grad-Shafranov equation is subsequently converged for each equilibrium with fixed coil positions, using further Picard iterations and constrained current optimisation (Equation 25).

Finally, in order to ensure that the breakdown phase constraints can still be met with the new, optimal coil locations and maximum PF coil current constraints, Equation 27 is recalculated.

6. Demonstration of capabilities

To demonstrate our approach we introduce a range of different equilibria and coilset designs, showing that our methodology is applicable to a variety of tokamak concepts. We present a single null (SN), double null (DN) and a single null, negative triangularity (NT) plasma and poloidal field system designs. The design points shown here are fairly arbitrary and are intended only to demonstrate the flexibility of our approach in handling significantly different configurations, see Table 2. All configurations are pulsed reactors, as this constitutes the harder optimisation problem. In all configurations, we assume Nb_3Sn coils for the CS coils and NbTi coils for the PF coils, and the PF coil exclusions zones are placed assuming a typical vertical maintenance approach.

Table 2: Reactor configuration parameters

	SN	DN	NT
R_0 [m]	9	6.8	8
A	3.1	2	3.3
κ	1.64	1.64	1.67
δ	0.29	0.3	-0.35
I_p [MA]	19	14	15
B_ϕ [T]	5.8	5.2	5.2
β_p [%]	1.34	0.73	1.25
l_i	0.8	0.7	0.8
τ_{ft} [hr]	2	0.5	1.1
n_{PF}	6	6	5
n_{CS}	5	7	6
$F_{PF_{max}}$ [MN]	400	300	350
$F_{CS_{tot_{max}}}$ [MN]	300	200	300
$F_{CS_{sep_{max}}}$ [MN]	200	200	250

We use a spline TF coil shape basis function for the large SN reactor, six PF coils and a standard EU-DEMO-like division of the CS into five modules, see Figure 3 and Table 3.

For the smaller and tighter aspect ratio DN reactor (Figure 4 and Table 4), we use a "Princeton D" TF coil shape as a basis function, and seven divisions on the CS as this is useful in controlling the positions of the inboard divertor legs.

For the NT reactor (Figure 5 and Table 5), we use a "picture frame" TF coil shape, as we consider this to be an appropriate design choice for such a reactor. We choose to use only four CS divisions and five PF coils, to demonstrate that the approach can handle different numbers of coils, and to show that a NT reactor need not have as many PF coils as has sometimes been assumed (such as in [9]). It is worth mentioning that a higher breakdown flux and longer pulse length (whilst preserving the prescribed plasma shape) could be achieved in this NT reactor, were more PF coils to be used.

7. Discussion and future work

The equilibria and poloidal field system design optimisation procedure described here takes approximately three to four minutes to run from start to finish (including generating and converging all the equilibria) on a single Intel® i-7 processor on a desktop machine. This is prior to any concerted effort to optimise code performance, which will be the subject of future work. The run-time is dominated by the non-linear optimisation procedures, and to a lesser extent the numerical calculation of plasma integral values. It can vary depending on the configuration and the convergence/stopping criteria applied in the optimisation steps. In practice, different configurations require slightly different optimisation parameters, numbers of constraints, etc. Thus the procedure cannot yet be described as "fully automated" in all cases, as user experience and understanding, as well as some elements of trial and error are required in order to design a suitable coilset and equilibria. For reasonable parameter deviations around known machines, however, automated (that is to say, fully unsupervised) equilibria and poloidal field system design is possible.

It should also be noted that the specification of reasonable and self-consistent constraints is important to the success of the optimisation routines.

Future work will focus on the acceleration of the procedure and on the improvement of its robustness and automatability. We will also seek to extend coverage to include other magnetic configurations with more advanced divertor geometries, such as the SX and SF configurations.

8. Conclusions

The design of plasma equilibria and associated poloidal field systems is one of the very first activities to be carried out in the design of future fusion reactors.

To this end, we have described a free boundary plasma MHD equilibrium code, along with a set of novel design optimisation routines which enable the design of tokamak equilibria and poloidal field systems. A broad variety of constraints can be met, ranging from plasma shape constraints (R_0, A, κ, δ), integral plasma constraints (I_p, β_p, l_i), a pulse length constraint (τ_{ft}), and engineering constraints relating to the locations, currents, fields, and forces in the coils ($\mathbf{L}, \mathbf{I}, \mathbf{B}, \mathbf{F}$). The approach has been demonstrated on indicative single-null, double-null, and negative triangularity tokamak designs. The methodology is integrated into the BLUEPRINT reactor design framework, and runs within minutes, thus making it compatible for use in global reactor design optimisation procedures.

Acknowledgements

We would like to thank Dr B. Dudson (University of York) for sharing FreeGS with the wider community, as it has been extremely useful in developing our work; Dr G. Cunningham (UKAEA) for his wise words, advice, and sharing FIESTA with us, which has also been of great help; Dr. F. Maviglia (EUROfusion) and Dr. F. Franza (KIT) for their advice and expertise; E. Jensen for her English; and Dr G. Parks (University of Cambridge) and Dr E. Surrey (UKAEA) for their mentorship, support, wise words and guidance.

This work has been funded by the RCUK Energy Programme [grant number EP/I501045]. To obtain further information on the data and models underlying this paper please contact PublicationsManager@ccfe.ac.uk.

Appendix 1: Green's functions and discretised coils

The Green's functions for poloidal magnetic flux, radial magnetic field, and vertical magnetic field at a location (X, Z) due to a unit current source at location $\mathbf{P} \equiv (X_c, Z_c)$:

$$\mathcal{G}^{\mathbf{P}}_{\psi}(X,Z) = \frac{\mu_0}{2\pi} a[(1-k/2)\mathrm{K}(k) - \mathrm{E}(k)] \tag{31}$$

$$\mathcal{G}^{\mathbf{P}}_{B_x}(X,Z) = \frac{\mu_0}{2\pi} \frac{(Z-Z_c)(T_2[(Z-Z_c)^2 + X^2 + X_c^2] - T_1)}{X} \tag{32}$$

$$\mathcal{G}^{\mathbf{P}}_{B_z}(X,Z) = \frac{\mu_0}{2\pi}\left[T_1 + \left(X_c^2 - X^2 - (Z-Z_c)^2\right)T_2\right] \tag{33}$$

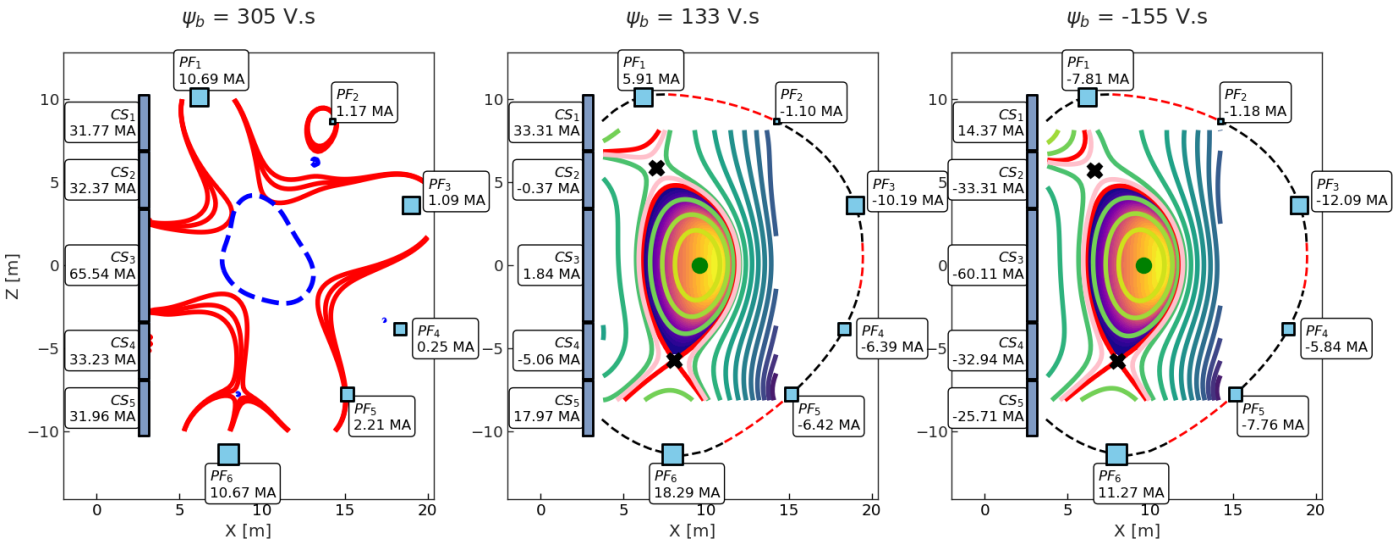

Figure 3: Indicative SN result showing the breakdown (left) the start of flat-top (centre) and end of flat-top (right) phases with an optimised poloidal field system. The contour lines show the magnetic flux surfaces, and the filled contour region shows the location of the plasma current density (zero outside the plasma), with in both cases lighter colours indicating higher values. The red contour lines are the separatrices (and the isoflux values near $\psi_{b_{BD}}$ in the case of the breakdown phase), and the pink contour lines show the flux surfaces with $\overline{\psi} = 1.05$. The green "O" and black "X" markers indicate O- and X-points, respectively. The red and black dashed lines show the basis function for the optimisation of the coil positions, with the red portions indicating the forbidden zones. The blue dashed line in the breakdown phase shows the zones where $B_p \leq 3$ mT.

Table 3: SN results for the constrained current optimisation procedure with optimal coil locations at the breakdown (BD), start of flat-top (SOF), and end of flat-top (EOF) phases, as shown in Figure 3. NOTE: PF coil current constraints were updated based on maximum currents throughout the three phases in order to converge coil cross-sectional areas.

	I [MA]				**B** [T]				**F$_z$** [MN]			
	$\lvert I_{max}\rvert$	BD	SOF	EOF	B_{max}	BD	SOF	EOF	$\lvert F_{z_{max}}\rvert$	BD	SOF	EOF
PF_1	14.53	10.69	5.91	-7.81	11.50	5.13	1.81	4.31	400.00	-287.88	-41.29	54.57
PF_2	1.18	1.17	-1.10	-1.18	11.50	1.54	1.92	2.00	400.00	-13.01	17.43	18.78
PF_3	12.96	1.09	-10.19	-12.09	11.50	1.46	3.82	4.44	400.00	-2.90	74.63	88.52
PF_4	6.39	0.25	-6.39	-5.84	11.50	0.66	3.71	3.36	400.00	0.78	-54.45	-49.69
PF_5	7.76	2.21	-6.42	-7.76	11.50	1.71	3.93	4.52	400.00	22.98	-102.29	-123.59
PF_6	18.29	10.67	18.29	11.27	11.50	5.33	6.06	3.56	400.00	298.58	150.15	92.47
CS_1	33.31	31.77	33.31	14.37	13.00	11.78	9.09	1.88	N/A	-638.04	-68.69	-29.64
CS_2	33.31	32.37	-0.37	-33.31	13.00	12.43	2.32	11.49	N/A	-72.24	1.07	95.52
CS_3	66.62	65.54	1.84	-60.11	13.00	12.78	1.40	12.91	N/A	-7.74	-0.02	0.81
CS_4	33.31	33.23	-5.06	-32.94	13.00	12.62	1.81	12.10	N/A	82.85	-14.46	-94.14
CS_5	33.31	31.96	17.97	-25.71	13.00	11.77	5.55	8.81	N/A	626.24	37.31	-53.37

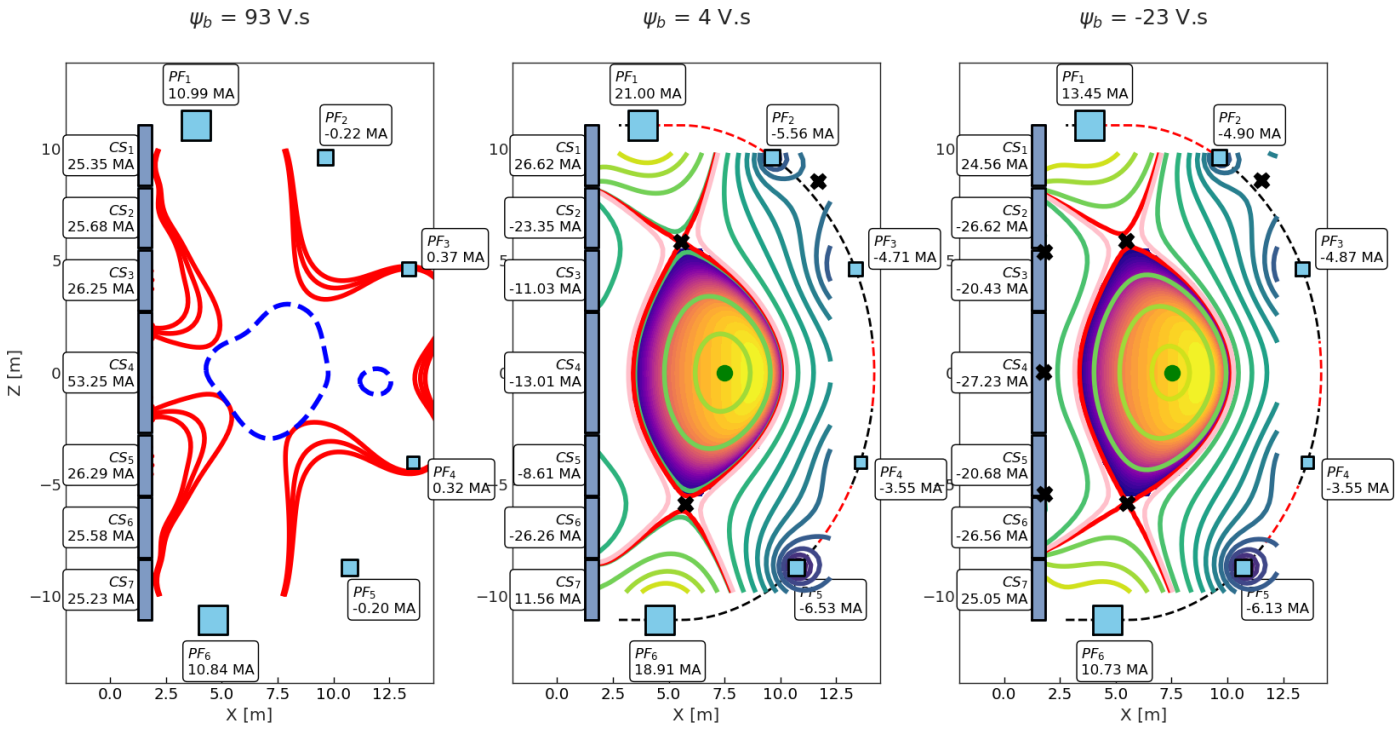

Figure 4: Indicative DN result showing the breakdown (left) the start of flat-top (centre) and end of flat-top (right) phases with an optimised poloidal field system.

Table 4: DN results for the constrained current optimisation procedure with optimal coil locations at the breakdown (BD), start of flat-top (SOF), and end of flat-top (EOF) phases, as shown in Figure 4. NOTE: PF coil current constraints were updated based on maximum currents throughout the three phases in order to converge coil cross-sectional areas.

	I [MA]				**B** [T]				**F$_z$** [MN]			
	$\lvert I_{max}\rvert$	BD	SOF	EOF	B_{max}	BD	SOF	EOF	$\lvert F_{z_{max}}\rvert$	BD	SOF	EOF
PF_1	21.00	10.99	21.00	13.45	11.50	5.51	7.06	4.21	300.00	-137.59	-35.64	-22.84
PF_2	5.62	-0.22	-5.56	-4.90	11.50	0.74	3.86	3.43	300.00	0.64	40.25	35.45
PF_3	4.87	0.37	-4.71	-4.87	11.50	0.85	3.13	3.22	300.00	-0.49	39.98	41.39
PF_4	3.55	0.32	-3.55	-3.55	11.50	0.79	2.45	2.45	300.00	0.46	-27.72	-27.72
PF_5	6.84	-0.20	-6.53	-6.13	11.50	0.70	3.98	3.73	300.00	-0.58	-54.77	-51.43
PF_6	21.00	10.84	18.91	10.73	11.50	5.47	6.31	3.22	300.00	135.18	43.93	24.92
CS_1	26.62	25.35	26.62	24.56	13.00	12.48	11.30	9.29	N/A	-115.52	-10.98	-10.13
CS_2	26.62	25.68	-23.35	-26.62	13.00	12.61	8.16	10.24	N/A	7.25	17.35	19.78
CS_3	26.62	26.25	-11.03	-20.43	13.00	12.73	6.15	10.21	N/A	-4.30	10.89	20.18
CS_4	53.25	53.25	-13.01	-27.23	13.00	11.81	4.65	7.96	N/A	0.02	0.00	0.00
CS_5	26.62	26.29	-8.61	-20.68	13.00	12.73	5.47	10.30	N/A	5.33	-8.50	-20.42
CS_6	26.62	25.58	-26.26	-26.56	13.00	12.56	9.64	10.27	N/A	-5.48	-19.51	-19.73
CS_7	26.62	25.23	11.56	25.05	13.00	12.40	5.18	8.91	N/A	115.44	4.77	10.33

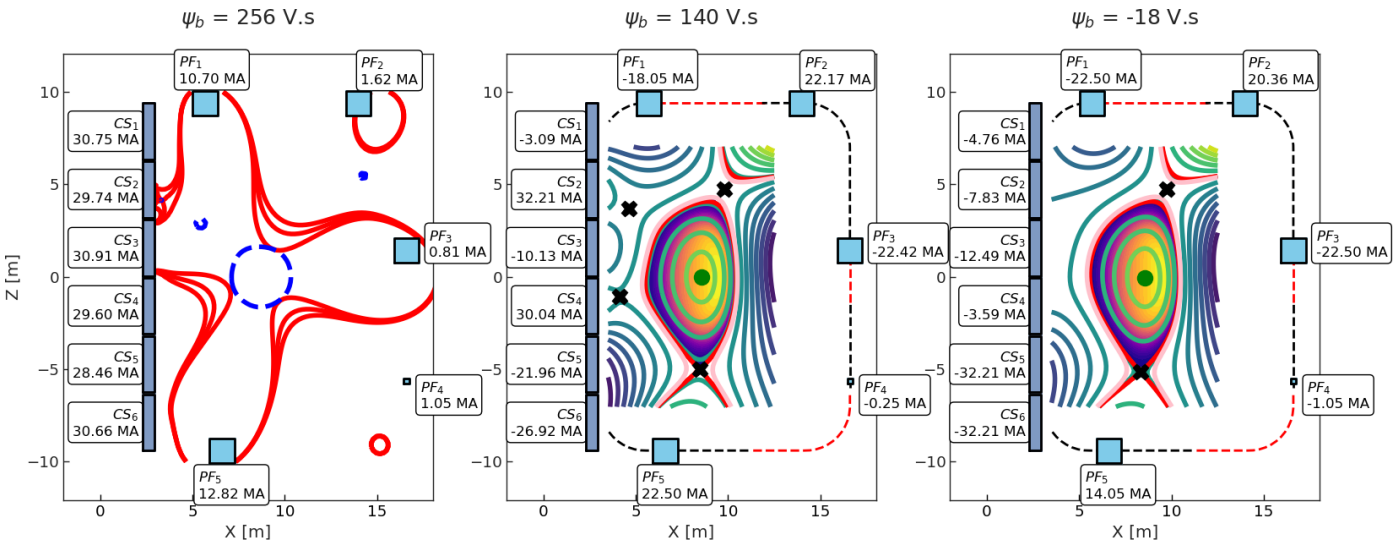

Figure 5: Indicative NT result showing the breakdown (left) the start of flat-top (centre) and end of flat-top (right) phases with an optimised poloidal field system.

Table 5: NT results for the constrained current optimisation procedure with optimal coil locations at the breakdown (BD), start of flat-top (SOF), and end of flat-top (EOF) phases, as shown in Figure 5. NOTE: PF coil current constraints were updated based on maximum currents throughout the three phases in order to converge coil cross-sectional areas.

	I [MA]				**B** [T]				**F$_z$** [MN]			
	$\|I_{max}\|$	BD	SOF	EOF	B_{max}	BD	SOF	EOF	$\|F_{z_{max}}\|$	BD	SOF	EOF
PF_1	22.50	10.70	-18.05	-22.50	11.50	5.25	5.76	7.61	350.00	-284.45	97.60	121.66
PF_2	22.17	1.62	22.17	20.36	11.50	1.84	6.50	5.98	350.00	-15.08	-211.36	-194.07
PF_3	22.50	0.81	-22.42	-22.50	11.50	1.27	6.67	6.67	350.00	0.50	70.06	70.30
PF_4	1.05	1.05	-0.25	-1.05	11.50	1.45	0.84	1.85	350.00	9.78	-2.06	-8.61
PF_5	22.50	12.82	22.50	14.05	11.50	5.77	7.68	4.78	350.00	334.78	155.67	97.21
CS_1	32.21	30.75	-3.09	-4.76	13.00	11.41	2.31	4.56	N/A	-535.54	5.03	7.75
CS_2	32.21	29.74	32.21	-7.83	13.00	11.65	9.35	5.02	N/A	-35.19	-74.04	18.00
CS_3	32.21	30.91	-10.13	-12.49	13.00	11.92	2.27	6.36	N/A	4.20	13.52	16.68
CS_4	32.21	29.60	30.04	-3.59	13.00	11.59	8.81	4.78	N/A	38.10	39.51	-4.72
CS_5	32.21	28.46	-21.96	-32.21	13.00	11.34	6.77	11.86	N/A	-0.04	-50.42	-73.95
CS_6	32.21	30.66	-26.92	-32.21	13.00	11.53	7.35	10.68	N/A	478.84	-44.09	-52.75

Where:

$$a \equiv \sqrt{(X + X_c)^2 + (Z - Z_c)^2} \tag{34}$$

$$k^2 \equiv \frac{4XX_c}{a^2} \tag{35}$$

$$T_1 \equiv \frac{\mathrm{K}(k)}{a} \tag{36}$$

$$T_2 \equiv \frac{\mathrm{E}(k)}{a^3(1-k)} \tag{37}$$

And K and E are the complete elliptic integrals of the first and second kind, respectively.

Note that the Green's functions diverge logarithmically when the measured point approaches the location of the source, $\mathbf{P}$. In practice, this is only an issue when calculating the self-field of a coil at its centre. For this we use a conservative approximation for the field inside a conductor; taking an average value of the field either side of the edge of the conductor.

A coil at position $\mathbf{P_C}$ is discretised into n_f individual current-carrying filaments at positions $\mathbf{p_i}$, each with the same current.

$$\mathcal{G}_v^{\mathbf{P_C}}(X, Z) = \frac{1}{n_f} \sum_i^{n_f} \mathcal{G}_v^{\mathbf{p_i}}(X, Z) \tag{38}$$

where:

v denotes one of $[\psi, B_x, B_z]$

$\mathbf{p_i}$ is the position of the subcoil i

In practice the coils are discretised based on their size (dx and dz), to accommodate rectangular shaped coils.

Appendix 2: plasma profile determination

From Equations 4 and 19, following [21] and FreeGS [22], we have:

$$\beta_p = \frac{8\pi}{\mu_0 I_p^2} \iint p dX dZ = -\frac{8\pi}{\mu_0 I_p^2} \frac{\lambda\beta_0}{R_0} \iint g \, dX dZ \tag{39}$$

thus

$$\lambda\beta_0 = -\frac{\beta_p I_p^2 R_0 \mu_0}{8\pi \iint g \, dX dZ} \tag{40}$$

giving

$$\lambda = \frac{I_p - \lambda\beta_0 \left(\iint \frac{X}{R_0} g \, dX dZ + \iint \frac{R_0}{X} g \, dX dZ \right)}{\iint \frac{R_0}{X} g \, dX dZ} \tag{41}$$

and

$$\beta_0 = \frac{\lambda\beta_0}{\lambda} \tag{42}$$

This enables the determination of two of the unknowns in Equation 4, λ and β_0, whilst ensuring that the I_p and β_p constraints are met.

Appendix 3: optimisation Jacobians

The vertical forces acting on the coils are calculated as:

$$\mathbf{F_z} = \mathbf{I} \circ (\mathbf{F_{a_z}} \cdot \mathbf{I} + \mathbf{F_{p_z}}) \tag{43}$$

where:

$\mathbf{F_z}$ is the n_C vector of the coil vertical forces

$\circ$ is the Hadamard product

$\mathbf{F_{a_z}}$ is the $n_C \times n_C$ response matrix of the active coil forces

$\mathbf{F_{p_z}}$ is the n_C response vector of the passive coil force contributions (including the plasma)

$$\begin{aligned} F_{a_{z_{i,j}}} &= -2\pi X_i \mathcal{G}_{B_x}^{\mathbf{P_j}}(X_i, Z_i) \\ F_{p_{z_i}} &= -2\pi X_i \sum_{k=1}^{n_P} I_k \mathcal{G}_{B_x}^{\mathbf{P_k}}(X_i, Z_i) \end{aligned} \tag{44}$$

where n_P is the number of passive coils (including the plasma, which is discretised into many small coils).

The poloidal fields at the coils locations are calculated as:

$$\mathbf{B} = \sqrt{(\mathbf{B_{a_x}}\mathbf{I})^{\circ 2} + (\mathbf{B_{a_z}}\mathbf{I})^{\circ 2}} + \mathbf{B_{p_p}} \tag{45}$$

where:

$\mathbf{B}$ is the n_C vector of the poloidal field values at the coils

$\mathbf{B_{a_x}}$ and $\mathbf{B_{a_z}}$ are the $n_C \times n_C$ coil response matrices of the radial and vertical fields

$\mathbf{B_{p_p}}$ is the n_C response vector of the passive coil poloidal field contributions (including the plasma)

Deterministic optimisation algorithms require information on the gradient of the objective function and constraints. In the absence of analytical gradients (Jacobian matrices) an optimiser will calculate gradients numerically, requiring significantly more evaluations of the objective function. Below we detail the calculation of the Jacobians for the objective function, vertical force, and poloidal field, which are used in the optimisation procedures described here.

The Jacobian of the objective function used in Equation 25:

$$\frac{\partial \|\mathbf{G^L I} - \mathbf{b_t} + \mathbf{b_p}\|_2^2 + \|\mathbf{\Gamma I}\|_2^2}{\partial \mathbf{I}} = 2\mathbf{G^{L\intercal} G^L I} - 2\mathbf{G^L}(\mathbf{b_t} - \mathbf{b_p}) + 2\mathbf{\Gamma I} \tag{46}$$

The Jacobian of the field calculation:

$$\frac{\partial \mathbf{B}}{\partial \mathbf{I}} = \frac{\mathbf{B_{a_x}} \mathbf{I} \circ \mathbf{B_{a_x}} + \mathbf{B_{a_z}} \mathbf{I} \circ \mathbf{B_{a_z}}}{\sqrt{(\mathbf{B_{a_x}}\mathbf{I})^{\circ 2} + (\mathbf{B_{a_z}}\mathbf{I})^{\circ 2}}} \tag{47}$$

The Jacobian of the force calculation:

$$\frac{\partial \mathbf{F}}{\partial \mathbf{I}} = \mathbf{I}^{\intercal} \circ \mathbf{F_a} + \mathrm{diag}(\mathbf{I} \circ \mathrm{diag}(\mathbf{F_a}) + \mathbf{F_p}) \tag{48}$$

The gradients of the specific force and field inequality constraints with respect to $\mathbf{I}$ can be obtained from the above Jacobians.

References

[1] M. Kovari, R. Kemp, H. Lux, P. Knight, J. Morris, and D. J. Ward, "PROCESS: A systems code for fusion power plantsPart 1: Physics," *Fusion Engineering and Design*, vol. 89, pp. 3054–3069, Dec. 2014.

[2] C. Reux, L. D. Gallo, F. Imbeaux, J.-F. Artaud, P. Bernardi, J. Bucalossi, G. Ciraolo, J.-L. Duchateau, C. Fausser, D. Galassi, P. Hertout, J.-C. Jaboulay, A. Li-Puma, B. Saoutic, L. Zani, and I.-T. Contributors, "DEMO reactor design using the new modular system code SYCOMORE," *Nuclear Fusion*, vol. 55, no. 7, p. 073011, 2015.

[3] F. Franza, L. V. Boccaccini, U. Fisher, P. V. Gade, and R. Heller, "On the implementation of new technology modules for fusion reactor systems codes," *Fusion Engineering and Design*, vol. 98-99, pp. 1767–1770, Oct. 2015.

[4] M. Coleman and S. McIntosh, "BLUEPRINT: A novel approach to fusion reactor design," *Fusion Engineering and Design*, vol. 139, pp. 26–38, Feb. 2019.

[5] G. Federici, C. Bachmann, L. Barucca, W. Biel, L. Boccaccini, R. Brown, C. Bustreo, S. Ciattaglia, F. Cismondi, M. Coleman, V. Corato, C. Day, E. Diegele, U. Fischer, T. Franke, C. Gliss, A. Ibarra, R. Kembleton, A. Loving, F. Maviglia, B. Meszaros, G. Pintsuk, N. Taylor, M. Q. Tran, C. Vorpahl, R. Wenninger, and J. H. You, "DEMO design activity in Europe: Progress and updates," *Fusion Engineering and Design*, June 2018.

[6] R. Ambrosino, R. Albanese, G. Calabr, A. Castaldo, F. Crisanti, V. P. Loschiavo, M. de Magistris, S. Minucci, and G. Ramogida, "The DTT device: Poloidal field coil assessment for alternative plasma configurations," *Fusion Engineering and Design*, vol. 122, pp. 322–332, Nov. 2017.

[7] F. Subba, L. Aho-Mantila, R. Ambrosino, D. P. Coster, V. Pericoli-Ridolfini, A. Uccello, and R. Zanino, "Preliminary analysis of the efficiency of non-standard divertor configurations in DEMO," *Nuclear Materials and Energy*, vol. 12, pp. 967–972, Aug. 2017.

[8] M. Kikuchi, S. Medvedev, T. Takizuka, A. Fasoli, Y. Wu, P. Diamond, X. Duan, Y. Kishimoto, K. Hanada, L. Villard, O. Sauter, S. Coda, B. Duval, H. Reimerdes, S. Brunner, G. Merlo, J. Jiang, M. Wang, M. Ni, D. Chen, H. Du, W. Duan, Y. Hou, A. Ivanov, A. Martynov, Y. Poshekhonov, Y. Ueda, L. Yan, X. Song, G. Zheng, J. Liu, K. Nagasaki, K. Imadera, K. Mishra, A. Fujisawa, K. Nakamura, H. Zushi, M. J. Pueschel, X. Z. Xu, P. Hu, D. Told, G. Q. Li, M. Furukawa, T. Ozeki, K. Shimizu, K. Kawashima, H. Urano, M. Honda, T. Ando, and M. Kuriyama, "Perspective of Negative Triangularity Tokamak as Fusion Energy System," *Europhysics Conference Abstracts*, p. P4.179, 2015.

[9] S. Medvedev, M. Kikuchi, L. Villard, T. Takizuka, P. Diamond, H. Zushi, K. Nagasaki, X. Duan, Y. Wu, A. Ivanov, A. Martynov, Y. Poshekhonov, A. Fasoli, and O. Sauter, "The negative triangularity tokamak: stability limits and prospects as a fusion energy system," *Nuclear Fusion*, vol. 55, p. 063013, June 2015.

[10] J. Menard, T. Brown, L. El-Guebaly, M. Boyer, J. Canik, B. Colling, R. Raman, Z. Wang, Y. Zhai, P. Buxton, B. Covele, C. DAngelo, A. Davis, S. Gerhardt, M. Gryaznevich, M. Harb, T. Hender, S. Kaye, D. Kingham, M. Kotschenreuther, S. Mahajan, R. Maingi, E. Marriott, E. Meier, L. Mynsberge, C. Neumeyer, M. Ono, J.-K. Park, S. Sabbagh, V. Soukhanovskii, P. Valanju, and R. Woolley, "Fusion nuclear science facilities and pilot plants based on the spherical tokamak," *Nuclear Fusion*, vol. 56, p. 106023, Oct. 2016.

[11] K. Toi and T. Takeda, "Optimum Design of Control Coils in a Tokamak Device by Nonlinear Optimization," *Japanese Journal of Applied Physics*, vol. 16, pp. 325–334, Feb. 1977.

[12] T. Kobayashi, K. Tani, and S. Tamura, "Determination of Optimum Positions of the Poloidal Field Coils of a Large Tokamak," *Japanese Journal of Applied Physics*, vol. 17, pp. 2139–2146, Dec. 1978.

[13] D. J. Strickler, J. D. Galambos, and Y.-K. M. Peng, "MHD equilibrium methods for ITER PF coil design and system analysis," Tech. Rep. ORNL/FEDC-88/7, 1989.

[14] Z.-L. An, X.-P. Liu, B. Wu, and X.-J. Zha, "Optimization of Positions and Currents of Tokamak Poloidal Field Coils Using Genetic Algorithms," *Fusion Science and Technology*, vol. 50, pp. 561–568, Nov. 2006.

[15] R. Albanese, R. Ambrosino, A. Castaldo, and V. P. Loschiavo, "Optimization of the PF coil system in axisymmetric fusion devices," *Fusion Engineering and Design*, vol. 133, pp. 163–172, Aug. 2018.

[16] F. Franza, I. S. Landman, and S. Pestchanyi, "Development of an advanced magnetic equilibrium model for fusion reactor system codes," *Fusion Engineering and Design*, vol. 136, pp. 309–313, Nov. 2018.

[17] V. D. Shafranov, "On magnetohydrodynamical equilibrium configurations," *Journal of Experimental Theoretical Physics (U.S.S.R.)*, vol. 33, pp. 710–722, 1957.

[18] H. Grad and H. Rubin, "Hydromagnetic equilibria and force-free fields," *Journal of Nuclear Energy (1954)*, vol. 7, pp. 284–285, Sept. 1958.

[19] J. L. Luxon and B. B. Brown, "Magnetic analysis of non-circular cross-section tokamaks," *Nuclear Fusion*, vol. 22, pp. 813–821, June 1982.

[20] L. Lao, H. St. John, R. Stambaugh, A. Kellman, and W. Pfeiffer, "Reconstruction of current profile parameters and plasma shapes in tokamaks," *Nuclear Fusion*, vol. 25, pp. 1611–1622, Nov. 1985.

[21] Y. M. Jeon, "Development of a free-boundary tokamak equilibrium solver for advanced study of tokamak equilibria," *Journal of the Korean Physical Society*, vol. 67, pp. 843–853, Sept. 2015.

[22] B. Dudson, "FreeGS: Free boundary Grad-Shafranov solver," June 2019. https://github.com/bendudson/freegs.

[23] J. L. Johnson, H. E. Dalhed, J. M. Greene, R. C. Grimm, Y. Y. Hsieh, S. C. Jardin, J. Manickam, M. Okabayashi, R. G. Storer, A. M. M. Todd, D. E. Voss, and K. E. Weimer, "Numerical determination of axisymmetric toroidal magnetohydrodynamic equilibria," *Journal of Computational Physics*, vol. 32, pp. 212–234, Aug. 1979.

[24] R. Albanese and F. Villone, "The linearized CREATE-L plasma response model for the control of current, position and shape in tokamaks," *Nuclear Fusion*, vol. 38, pp. 723–738, May 1998.

[25] J. Johner, "HELIOS: A Zero-Dimensional Tool for Next Step and Reactor Studies," *Fusion Science and Technology*, vol. 59, pp. 308–349, Feb. 2011.

[26] J. Manickam, "Stability of n = 1 internal modes in tokamaks," *Nuclear Fusion*, vol. 24, pp. 595–608, May 1984.

[27] L. Zakharov, "Numerical methods for solving some problems of the theory of plasma equilibrium in toroidal configurations," *Nuclear Fusion*, vol. 13, pp. 595–602, Aug. 1973.

[28] K. Lackner, "Computation of ideal MHD equilibria," *Computer Physics Communications*, vol. 12, pp. 33–44, Sept. 1976.

[29] A. N. Tikhonov and V. I. Arsenin, *Solutions of ill-posed problems*. Winston, 1977.

[30] F. Hofmann, "FBT - a free-boundary tokamak equilibrium code for highly elongated and shaped plasmas," *Computer Physics Communications*, vol. 48, pp. 207–221, Feb. 1988.

[31] D. Kraft, "A Software Package for Sequential Quadratic Programming," Tech. Rep. DFVLR-FB 88-28, Deutsche Forschungs- und Versuchsanstalt fr Luft- und Raumfahrt, 1988.

[32] S. G. Johnson, "The NLopt nonlinear-optimization package," 2018.

[33] O. Crofts, A. Loving, D. Iglesias, M. Coleman, M. Siuko, M. Mittwollen, V. Queral, A. Vale, and E. Villedieu, "Overview of progress on the European DEMO remote maintenance strategy," *Fusion Engineering and Design*, vol. 109-111, pp. 1392–1398, Nov. 2016.

[34] L. M. Waganer, "ARIES-AT maintenance system definition and analysis," *Fusion Engineering and Design*, vol. 80, pp. 161–180, Jan. 2006.

[35] M. J. D. Powell, "A Direct Search Optimization Method That Models the Objective and Constraint Functions by Linear Interpolation," in *Advances in Optimization and Numerical Analysis* (S. Gomez and J.-P. Hennart, eds.), Mathematics and Its Applications, pp. 51–67, Dordrecht: Springer Netherlands, 1994.

[36] R. Ambrosino, G. D. Tommasi, M. Mattei, and A. Pironti, "Model based optimization and estimation of the field map during the breakdown phase in the ITER tokamak," in *2015 IEEE Conference on Control Applications (CCA)*, pp. 1284–1289, Sept. 2015.

[37] S. Ejima, R. Callis, J. Luxon, R. Stambaugh, T. Taylor, and J. Wesley, "Volt-second analysis and consumption in Doublet III plasmas," *Nuclear Fusion*, vol. 22, pp. 1313–1319, Oct. 1982.